Title

Sequentially coupled flow and geomechanical simulation with a discrete fracture model for analyzing fracturing fluid recovery and distribution in fractured ultra-low permeability gas reservoirs

Authors
Liu, Yongzan
Liu, Lijun
Leung, Juliana Y
et al.

Publication Date
2020-06-01

DOI
10.1016/j.petrol.2020.107042

Peer reviewed

Sequentially Coupled Flow and Geomechanical Simulation with a Discrete Fracture Model for Analyzing Fracturing Fluid Recovery and Distribution in Fractured Ultra-low Permeability Gas Reservoirs

Yongzan Liu[1,*], Lijun Liu[1,2,*], Juliana Y. Leung[3], George J. Moridis[1,4]

[1] Harold Vance Department of Petroleum Engineering, Texas A&M University, College Station, USA
[2] Research Center of Multiphase Flow in Porous Media, China University of Petroleum (East China), Qingdao, China
[3] Department of Civil and Environmental Engineering, University of Alberta, Edmonton, Canada
[4] Energy Geoscience Division, Lawrence Berkeley National Laboratory, Berkeley, USA
[*] Corresponding authors: yongzan@tamu.edu (Y. Liu) and liulijunupc@163.com (L. Liu)

Abstract

More accurate characterization and prediction of the in-situ distribution of fracturing fluid in fractured reservoirs are needed for enhancing well productivity. In this study, an implicit-sequentially coupled flow/geomechanics simulator incorporating an efficient discrete fracture model is developed to model fluid distribution and recovery performance of ultra-low permeability gas reservoirs. The finite-volume and finite-element methods are used for space discretization of the flow and geomechanics equations, respectively, while the backward Euler method is employed for time discretization. The flow and geomechanics equations are solved sequentially based on fixed-stress splitting. An efficient discrete-fracture model is used to explicitly model the fractured system. Flexible unstructured gridding is employed to model arbitrarily-oriented fractures. The interrelations among pore volume, permeability and geomechanical conditions are considered dynamically using two-way coupled flow and geomechanics computations.

The geometry of fracture (networks) due to hydraulic fracturing has significant impacts on the fracturing fluid recovery efficiency and ensuing fluid distribution. Under the same injection volume, the fracturing fluid recovery is higher when the fracture geometry is planar. Fluid recovery is relatively lower whenever natural fractures are activated during fracturing treatments; flowback time is also shortened when complex fracture network with enlarged fracture interface is present. Fracturing fluid in hydraulic fractures may leak off into the natural fractures and subsequently imbibes into the surrounding matrix due to capillarity effects. The fracturing fluid recovery and in-situ fluid distribution are sensitive to the shut-in duration and fracture closure behavior.

This study analyzes the coupled flow-geomechanical responses of fractured gas reservoirs during the post-fracturing periods. Understanding the fate of the fracturing fluid can provide insights on, to some extent, the stimulated fracture volume, size of the water invasion zone, and efficiency of the fracturing design. The simulation predictions can also provide more accurate initial reservoir conditions (e.g. distributions of different phases and pressure) for long-term well performance estimation.

Keywords: coupled flow and geomechanics; flowback; fracturing-fluid distribution; tight/shale gas; fracture geometry

Introduction

Shale or tight gas reservoirs have emerged in recent years as huge energy resources, and slick-water fracturing treatment is widely used in the economic development of such ultra-low permeability reservoirs; large volumes of water are injected into the subsurface formation to create highly conductive fractures (Palisch et al. 2010; Du and Nojabaei 2019). Field observations indicate that only a small portion of the injected water, ranging from 5 to 50% among different reservoirs, can be recovered during the flowback operations (King 2010; Abbasi et al. 2014). In many cases, less than half of the injected water can be recovered after one year of production (Moridis 2017). The water-loss mechanisms and their effects on gas production post flowback have been the subject of many recent research studies. Alkouh et al. (2014), Clarkson and Williams-Kovacs (2013), Yang et al. (2017), and Jia et al. (2017) developed several (semi-)analytical models to analyze flowback and early-time production data and concluded that flowback production patterns appear to be strong indicators of the in-situ fracture characteristics. However, due to their many simplifications and assumptions, there are limitations for simulating temporal and spatial variation of fracturing fluid distribution using these (semi-)analytical models. On the other hand, numerical simulation offers an alternative for capturing complex physical mechanisms, and it can be used to assess the various influencing factors and predict the in-situ fluid distributions under various scenarios. Several numerical studies indicate that high capillary pressure and low water relative permeability are responsible for high water retention in the matrix, resulting in low water recoveries (Gdanski et al. 2009; Wang et al. 2010; Cheng 2012; Bertoncello et al. 2014; Yue et al. 2016). The injected water could also leak off into the surrounding natural or secondary fractures (Fan et al. 2010; Cheng 2012). Matrix imbibition could drive the imbibed water farther into the formation, although this process is quite slow (Wang and Leung 2015). A particular limitation in these aforementioned studies is that relatively coarse spatial discretization was used, where the discontinuity in saturation across a fracture face was not captured precisely.

In addition to capillarity and fluid flow effects, dramatic changes in the pressure and phase saturation during the hydraulic fracturing process and subsequent flowback or production stages would directly influence the geomechanical response, which affects the porosity and permeability of the system (Rutqvist and Stephansson 2003). Liu et al. (2019) conducted a series of simulation studies to investigate the impacts of fracture closure and observed that fracture closure would cause more water to imbibe into the matrix; although their study highlighted the importance of incorporating dynamic fracture properties, the mechanism of fracture closure was modeled based on certain empirical correlations describing fracture permeability or aperture as functions of fluid pressure; geomechanics calculations were omitted and the total stress acting on fracture surface was assumed to be constant; matrix deformation was also ignored. A detailed two-way coupled flow and geomechancis models that would fully capture the dynamic interrelations among pore/fracture volume, matrix permeability/fracture conductivity is rarely used to examine fracturing fluid distribution and recovery.

The overall fracture-matrix interface is affected by the overall fracture (network) geometries, which are functions of fluid flow and geomechanics. Understanding the fracturing fluid flowback patterns and recoveries may help reducing uncertainties associated with the identification and characterization of the fractured system (Clarkson and Williams-Kovacs 2013; Abbasi et al. 2014; Moridis 2017). Li et al. (2016; 2017) simulated tracer flowback profiles in stochastically generated fracture networks, and the results revealed that tracer flowback data analysis could be a promising technique to characterize stimulated fracture networks. Ehlig-Economides and Economides (2011) suggested that unrecovered fracturing fluid in the hydraulic fracture could activate nearby natural fractures, which behave like a propped fracture and enable gas flow; their results seem to suggest that low fracturing fluid recovery could be an indication of activation of natural fractures. Mukuhira et al. (2016) also reported that high pressure near the injection point would diffuse to the surrounding formation, activating natural fractures or other discontinuities along the way during the subsequent shut-in period. Kumar et al. (2018) discovered a positive correlation between prolonged seismic events and well productivity, corroborating the proposed mechanisms regarding the diffusion of hydrofracturing fluid into the surrounding matrix and activation of pre-existing gas-saturated natural fractures. Therefore, to fully examine the fate of fracturing fluid and its effects on the stimulated fracture volume, discrete fracture models, where individual fractures are modeled explicitly, coupled with unstructured gridding techniques, should be implemented for high-resolution investigation of multiphase flow in unconventional reservoirs (Karimi-Fard et al. 2004).

In summary, a coupled multiphase flow and geomechanics simulation model capable of handling complex fracture networks is needed to analyze fracturing fluid distribution and flowback at high resolution. An improved understanding of the relationship between flowback patterns and fracture network geometries is beneficial for the identification and characterization of hydraulically fractured systems. The main objective of this study is developing a sequentially coupled multiphase flow and geomechanics simulator, where an efficient discrete fracture model is incorporated, to examine the fracturing fluid distribution and flowback characteristics for a variety of fracture configurations. Relationships between flowback behavior and connected fracture systems are inferred.

Mathematical formulation

Governing Equations for Fluid Flow – The mass balance for component *k* is written as follows:

$$\frac{d}{dt}\int_{\Omega} m^k d\Omega + \int_{\Gamma} \mathbf{f}^k \cdot \mathbf{n} d\Gamma = \int_{\Omega} q^k d\Omega \quad \text{.......................................}(1)$$

where the superscript *k* indicates the component. $d(\cdot)/dt$ represents the time derivative of a physical quantity $(\cdot)$. m^k is mass of component *k*. $\mathbf{f}^k$ and q^k are the flux and source terms on the physical domain Ω with a boundary Γ, respectively, and $\mathbf{n}$ is the outer normal vector of the boundary. The mass of component *k* is written as:

$$m^k = \sum_J \phi S_J \rho_J X_J^k + \delta_s (1-\phi) \rho_R \gamma^k \quad \text{.......................................}(2)$$

where the subscript J indicates the fluid phase. ϕ is the true porosity, defined as the ratio of the pore volume to the bulk volume in the deformed configuration. S_J and ρ_J are saturation and density of phase J, respectively, and X_J^k is the mass fraction of component k in phase J. δ_s is an indicator for gas sorption. $\delta_s = 0$ for non-sorb rock, such as a typical tight gas formation, while $\delta_s = 1$ for gas-sorb rock, such as shales. ρ_R is the rock density, and γ^k is the mass of sorbed component k per unit mass of rock. The mass flux term is described as:

$$\mathbf{f}^k = \sum_J \mathbf{w}_J^k = \sum_J X_J^k \mathbf{w}_J \quad \text{.......................................}(3)$$

where $\mathbf{w}_J^k$ is the convective mass flow of component k in phase J. The diffusive mass flow is ignored in this model. The phase mass flow $\mathbf{w}_J$ is given by Darcy's Law according to the following equation:

$$\mathbf{w}_J = -\frac{\rho_J k_{rJ}}{\mu_J} \mathbf{k}\left(\mathbf{Grad} p_J - \rho_J \mathbf{g}\right) \quad \text{.......................................}(4)$$

where $\mathbf{k}$ is the absolute permeability tensor. μ_J and k_{rJ} are the viscosity and relative permeability of phase J, respectively. p_J is the fluid pressure of phase J, and $\mathbf{g}$ is the gravity vector, and **Grad** is the gradient operator.

Governing Equations for Geomechanical Responses – The quasi-static momentum conservation equation is written as:

$$\nabla \bullet \sigma + \rho_b \mathbf{g} = \mathbf{0} \quad \text{.......................................}(5)$$

where $\boldsymbol{\sigma}$ is the total stress tensor, and ρ_b is the bulk density. Infinitesimal deformation is assumed, such that the strain tensor ($\boldsymbol{\varepsilon}$) can be calculated as a function of the displacement vector **u**:

$$\boldsymbol{\varepsilon} = \frac{1}{2}\left(\nabla \mathbf{u} + \nabla^T \mathbf{u}\right) \quad \text{.......................................}(6)$$

Boundary Conditions. The boundary conditions for the coupled problem are:

$$\mathbf{w}_J \cdot \mathbf{n}_f = \overline{w_J} \text{ on } \Gamma_f, \; p_J = \overline{p_J} \text{ on } \Gamma_p, \quad \text{.......................................}(7)$$

$$\boldsymbol{\sigma} \cdot \mathbf{n}_t = \bar{t} \text{ on } \Gamma_t, \; \mathbf{u} = \overline{\mathbf{u}} \text{ on } \Gamma_u, \quad \text{.......................................}(8)$$

$$\boldsymbol{\sigma} \cdot \mathbf{n}_{HF} = -\mathbf{t}_f \text{ on } \Gamma_{HF} \quad \text{.......................................}(9)$$

Γ_f and Γ_p are fixed flow rate ($\overline{w_J}$) flow boundary and fixed pressure ($\overline{p_J}$) flow boundary, where $\Gamma_f \cap \Gamma_p = \varnothing$ and $\Gamma_f \cup \Gamma_p = \partial\Omega$; Γ_t and Γ_u are fixed traction ($\bar{t}$) geomechanical boundary and fixed displacement ($\bar{\mathbf{u}}$) geomechanical boundary, where $\Gamma_t \cap \Gamma_u = \varnothing$ and $\Gamma_t \cup \Gamma_u = \partial\Omega$; $\partial\Omega$ denotes the outer boundary of the whole domain. $\mathbf{n}_t$ and $\mathbf{n}_f$ are unit normal vector to Γ_t and Γ_f, respectively. Fractures act as internal boundaries (Γ_{HF}), as shown in **Figure 1**. The traction acting on fracture surface ($\mathbf{t}_f$) can be expressed as:

$$\mathbf{t}_f = \left(p_{HF} + p_s \right) \cdot \mathbf{n}_{HF} \quad \text{...}(10)$$

where the fluid pressure in fractures (p_{HF}) is exerted on the internal boundaries, where $\mathbf{n}_{HF}$ is the unit normal vector to Γ_{HF} pointing from Γ_{HF}^- to Γ_{HF}^+ . p_s is the force acting on the fracture faces due to compression of the proppant pack. Assuming that the proppant pack behaves linear-elastically under compression, p_s can be written as (Yan et al. 2018):

$$p_s = \begin{cases} -E_s \left(\mathbf{u}^+ - \mathbf{u}^- \right) \cdot \mathbf{n}_{HF} / d_{HF,0}, & \left(\mathbf{u}^+ - \mathbf{u}^- \right) \cdot \mathbf{n}_{HF} < 0 \\ 0, & \left(\mathbf{u}^+ - \mathbf{u}^- \right) \cdot \mathbf{n}_{HF} \geq 0 \end{cases} \quad \text{...}(11)$$

where E_s is the Young's modulus of proppant pack. $\left(\mathbf{u}^+ - \mathbf{u}^- \right) \cdot \mathbf{n}_{HF}$ represents the normal displacement jump between fracture faces (i.e. aperture changes), and $d_{HF,0}$ is the initial fracture aperture.

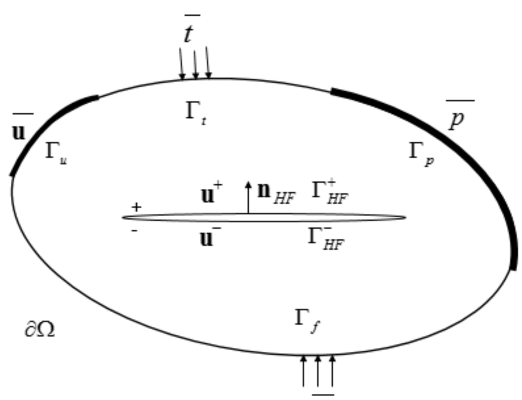

Figure 1 Schematic of a fractured porous medium and its boundaries.

Constitutive Relations. With the sign convention of tensile stress being positive, the constitutive relation for the rock skeleton can be written as:

$$\boldsymbol{\sigma} = \boldsymbol{\sigma}' - b\mathbf{I}p = \mathbf{C} : \boldsymbol{\varepsilon} - b\mathbf{I}p \quad \text{...}(12)$$

where b is the Biot's coefficient, $\boldsymbol{\sigma}$ and $\boldsymbol{\sigma}'$ are the total stress tensor and effective stress tensor, respectively. $p=\sum_J s_J p_J$ is the fluid pressure in multiphase flow. $\mathbf{C}$ is the elasticity tensor, which, in 2D plane-strain condition, is expressed as:

$$\mathbf{C}=\frac{E(1-\nu)}{(1+\nu)(1-2\nu)}\begin{bmatrix} 1 & \frac{\nu}{1-\nu} & \frac{\nu}{1-\nu} \\ \frac{\nu}{1-\nu} & 1 & \frac{\nu}{1-\nu} \\ \frac{\nu}{1-\nu} & \frac{\nu}{1-\nu} & 1 \end{bmatrix}$$

Following the fixed stress splitting algorithm (Mikelic and Wheeler, 2013), the flow problem is solved first to obtain p at the next time level (p^{n+1}) by freezing the total stress (i.e. $\delta\sigma_v=0$). According to Geertsma (1957), the true porosity variation in a deformable porous medium can be approximated as:

$$\delta\phi=\phi\left[\frac{1}{\phi}\left(\frac{1}{K_b}-\frac{1}{K_s}\right)-\frac{1}{K_b}\right](\delta\sigma_v+\delta p)=\phi\left[\frac{1}{\phi}\frac{b}{K_b}-\frac{1}{K_b}\right](\delta\sigma_v+\delta p) \quad \text{......................................(13)}$$

where K_b and K_s are the bulk modulus of the skeleton and modulus of the solid grain, respectively, and $b=1-\frac{K_b}{K_s}$ is the Biot's coefficient (Biot, 1941). With the constraint of $\delta\sigma_v=0$, the true porosity variation can be expressed as:

$$\delta\phi=\left(\frac{b-\phi}{K_b}\right)\delta p \rightarrow \phi^k=\phi^{k-1}+\frac{\left(b-\phi^{k-1}\right)}{K_b}\delta p^{k-1} \quad \text{......................................(14)}$$

where k refers to the Newton iteration counter. Substituting the relation between reservoir porosity ($\phi*$) and true porosity, i.e., $\phi*=\phi(1+\varepsilon_v)$, into the above equation gives:

$$\phi*^k=\phi*^{k-1}+\left[\frac{b(1+\varepsilon_v)-\phi*^{k-1}}{K_b}\right]\delta p^{k-1} \quad \text{......................................(15)}$$

The fixed stress splitting offers a framework for facilitating the evolution of reservoir porosity with both the volumetric strain and pore pressure, as prescribed by the flow problem solution. The matrix and fracture permeabilities are functions of the updated porosity:

$$k_m=k_{m0}\left(\frac{\phi_m^*}{\phi_0^*}\right)^n \quad \text{......................................(16)}$$

where k_m and ϕ_m^* are the matrix permeability and reservoir porosity, and the subscript "0" refers to the initial state. The fracture conductivity (F_f) is formulated according to the cubic law (Witherspoon et al. 1980):

$$F_f = F_{f0}\left(\frac{a_f}{a_{f0}}\right)^3 \quad \text{.......(17)}$$

where a_f are the fracture aperture.

Next, the geomechanics problem is solved freezing the fluid pressure. Invoking the porosity variation equation [Eq. (13)] and incorporating the relationship between volumetric stress and volumetric strain $\delta\sigma_v = K_b\delta\varepsilon_v - b\delta p$ (Biot, 1941) gives:

$$\delta\phi = (b-\phi)\delta\varepsilon_v + \frac{(b-\phi)(1-b)}{K_b}\delta p \quad \text{.......(18)}$$

Following the arguments of Coussy (2004), $(b-\phi)$ and $\frac{(b-\phi)(1-b)}{K_b}$ can be treated as constants in linear poroelasticity. Thus, integration of Eq. (18) from the initial state gives:

$$\phi - \phi_0 = (b-\phi_0)(\varepsilon_v - \varepsilon_{v0}) + \frac{(b-\phi_0)(1-b)}{K_b}(p-p_0) \quad \text{.......(19)}$$

With the relationship for reservoir porosity: $\phi^* = \phi(1+\varepsilon_v)$, Eq. (19) can be formulated as:

$$\begin{aligned}\phi^* &= \phi_0 + b(\varepsilon_v - \varepsilon_{v0}) + \frac{(b-\phi_0)(1-b)}{K_b}(p-p_0) + O(\varepsilon_v^2) \\ &\approx \phi_0 + b(\varepsilon_v - \varepsilon_{v0}) + \frac{(b-\phi_0)(1-b)}{K_b}(p-p_0)\end{aligned} \quad \text{.......(20)}$$

where $O(\varepsilon_v^2)$ term is neglected under the assumption of infinitesimal deformation (Dana et al., 2018).

Discretization and Solution Scheme

In this section, the numerical strategies for solving the coupled problem are presented. The grid structure is described first, and it is followed by a discussion of the finite volume discretization and finite element discretization for the flow and geomechanics problems, respectively. The mixed finite volume and finite element (MFVFE) formulation leads to a set of coupled nonlinear system of equations, which are solved sequentially using the fixed-stress splitting algorithm.

Grid Structure. The fractures are expressed explicitly using conformal unstructured grids. A fracture is treated as an interface element between its two neighboring matrix cells. As shown in **Figure 2,** a control volume is assigned to each element for the flow problem; the unknowns (i.e., p) are associated with the cell center. For the geomechanics problem, the unknowns (i.e., $\mathbf{u}$) are located at the element nodes. A splitting-node technique is used to duplicate the nodes along the fractures: each node has its own degrees of freedom, but it shares the same coordinates as the other split nodes (Ji et al. 2009; Garipov et al. 2016). The linear or nonlinear interactions of fracture surfaces and fracture-proppant can be easily implemented using this technique (Jiang and Yang 2018). These split nodes form the so-called 'zero-thickness interface element' that is widely applied in fracture mechanics, such as the cohesive zone model.

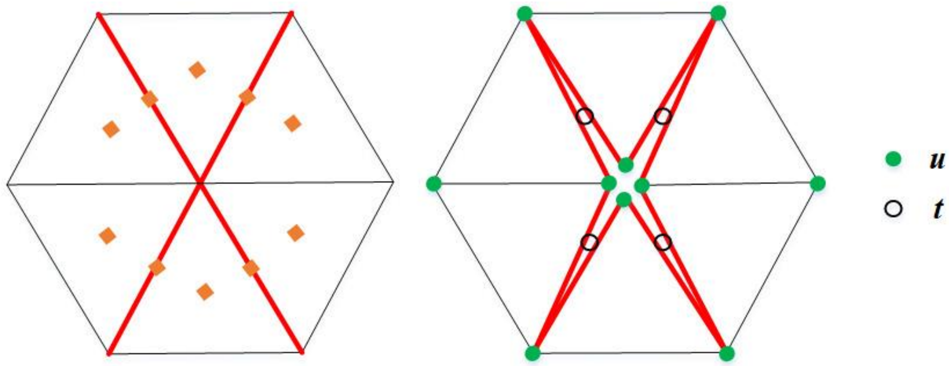

Figure 2 Grid structure for the flow (left) and geomechanics (right) problems [adapted from Garipov et al. (2016)]. Red lines represent fractures.

Finite-Volume Discretization of Flow Equation. Using a two-point flux approximation, the flow rate between two neighboring cells can be expressed as:

$$Q_{12} = T_{12}\lambda\left(p_2 - p_1\right) \quad \text{.......(21)}$$

where Q_{12} is flow rate from cell 1 to cell 2. T_{12} is the geometric part of the transmissibility, and λ represents the fluid mobility. The geometric part of the transmissibility is independent of the fluid phases, only depending on the geometry and intrinsic rock properties. In multiphase flow, the mobility part of the transmissibility of each phase is different, which is calculated based on upstream weighting.

An efficient discrete fracture model proposed by Karimi-Fard et al. (2004) is employed. The geometric part of the transmissibility is given by:

$$T_{12} = \frac{\alpha_1\alpha_2}{\alpha_1 + \alpha_2} \text{ with } \alpha_i = \frac{A_i k_i}{D_i}\mathbf{n}_i \cdot \mathbf{f}_i \quad \text{.......(22)}$$

where A_i is the area of the shared interface between the two cells, k_i is the permeability of cell *i*, D_i is the distance between the centroid of the shared face and the centroid of cell *i*, $\mathbf{n}_i$ is the unit vector normal to the interface pointing towards cell *i*, and $\mathbf{f}_i$ is the unit vector along the direction of the line connecting the cell centroid and interface centroid.

For a fracture intersection with *n* connected fracture segments, the geometric transmissibility between each pair of fracture segments (for example, cell *i* and cell *j*) can be approximated as:

$$T_{ij} \simeq \frac{\alpha_i \alpha_j}{\sum_{k=1}^{n} \alpha_k} \quad \text{.......}(23)$$

Finite-Element Discretization of Geomechanical Equation. Galerkin finite element method (FEM) is used to discretize the geomechanical equation. Linear triangular elements are used, and fluid pressure is constant within each element. Multiplying Eq. (12) by an arbitrary weighting function $\delta\mathbf{u}$, such that $\delta\mathbf{u}=0$ on the fixed displacement boundaries (Γ_u) and integrating Eq. (5) over the computational domain, the weak form of the geomechanical governing equation can be derived after applying divergence theorem:

$$\int_\Omega (\nabla\delta\mathbf{u})^T \sigma' d\Omega - \int_\Omega (\nabla\delta\mathbf{u})^T bp\mathbf{m} d\Omega + \int_{\Gamma_f} (\delta\Delta)^T \mathbf{t}_f d\Gamma = \int_{\Gamma_t} (\delta\mathbf{u})^T \bar{\mathbf{t}} d\Gamma + \int_\Omega (\delta\mathbf{u})^T \rho_b \mathbf{g} d\Omega \quad \text{.......}(24)$$

where $\mathbf{m}=[1,\ 1,\ 0]^T$ in 2D and $\mathbf{m}=[1,\ 1,\ 1,\ 0,\ 0,\ 0]^T$ in 3D. Δ represents the local separation of the fracture elements. The displacement unknowns are interpolated by multiplying the nodal values with the shape functions, as expressed in Eq. (25):

$$\mathbf{u} = \mathbf{N}\underline{\mathbf{u}} \quad \text{.......}(25)$$

where $\underline{\mathbf{u}}$ is the nodal displacement vector; $\mathbf{N}$ is a matrix consisting of the shape functions, which are the same to the weighting functions in Galerkin FEM. The relation between the local separation and global nodal displacement can be expressed as:

$$\Delta = \underbrace{\mathbf{NLR}}_{\mathbf{B_c}}\underline{\mathbf{u}} \quad \text{.......}(26)$$

where $\mathbf{N}$ is the shape function array of 1-D linear element; $\mathbf{L}$ is local displacement-separation relation matrix; $\mathbf{R}$ is the rotation matrix. The production of the three matrices forms the global displacement-separation relation matrix ($\mathbf{B_c}$). Detailed formulations can be found in Park and Paulino (2012). The discretized equation in matrix-vector form after neglecting the body force term in 2D becomes:

$$\mathbf{K}\underline{\mathbf{u}} - \mathbf{Q} + \mathbf{f}_f = \mathbf{f}_{\mathbf{ext}} \tag{27}$$

where,

$$\mathbf{K} = \int_\Omega (\nabla\mathbf{N})^T \mathbf{C}(\nabla\mathbf{N})\,d\Omega \tag{28}$$

$$\mathbf{Q} = \int_\Omega (\nabla\mathbf{N})^T bp\mathbf{m}\,d\Omega \tag{29}$$

$$\mathbf{f}_f = \int_{\Gamma_f} \mathbf{B_c}^T \mathbf{t}_f^k\,d\Gamma \tag{30}$$

$$\boldsymbol{f}_{ext} = \int_\Gamma \boldsymbol{N}^T \bar{\boldsymbol{t}}\,d\Gamma \tag{31}$$

Solution Strategy. The fixed-stress split iterative scheme decouples the flow problem and geomechanics problem, solving them sequentially at each time step. As shown in **Figure 3,** in each time step, the flow problem is solved first, and the porosity is updated during each Newton iteration *k*. Once the flow problem has converged (i.e., ||residual|| < tolerance), the geomechanical equation is solved using the updated fluid pressures. The reservoir porosity is computed again after the geomechanics problem is obtained. Finally, convergence for the entire coupled problem is checked: if the maximum relative error for the fluid pressure between coupling iterations is within a certain tolerance, the algorithm would proceed to the next time step; otherwise, the entire fixed-stress splitting iteration is repeated within the current time step.

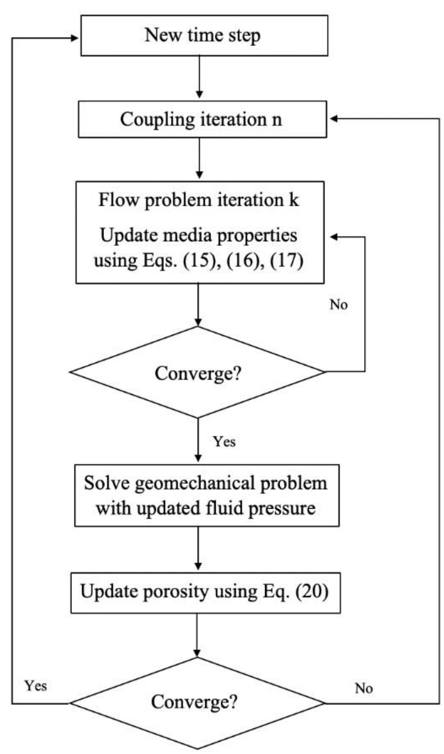

Figure 3 Flowchart of the sequential-implicit algorithm (each sub-problem, i.e., flow problem and geomechanical problem, is solved implicitly) for coupled flow and geomechanics based on fixed-stress splitting. The coupling convergence criterion is set as max{|| (p^{n+1}-p^n)/ p^{n+1}||}<10^{-5}.

Model Validation

Validation Case 1 – Water-gas two-phase flow. A case consisting of two sets of fractures for a domain of 10m×10m is constructed to validate the implementation of discrete fracture modeling, as shown in **Figure 4(a)**. An injector is placed at the left-bottom corner, where water is injected at a rate of 0.005 kg/s; a producer is located at the right-top corner with a constant flowing bottom-hole pressure of 25 MPa. At the initial conditions, p_0 = 35 MPa, ϕ_{m0} = 0.2, ϕ_f = 0.8, k_{m0} = 10 mD, and k_{f0} = 20 D (with an initial aperture of a_{f0} = 0.01 m), and constant water saturation of 0.2. The water saturation distributions at different times are shown in **Figure 4(b)**. The water saturation distributions predicted with the proposed model are in good agreement with those obtained from the commercial simulator GEM (GEM, 2015), validating the implementation of the discrete fracture model. In this simulation case, there are a total of 6665 elements (i.e. 13330 degrees of freedom in each iteration). With a single processor, the average CPU time for each Newton iteration is 2.3 seconds, and the average number of Newton iterations in each time step required for convergence is 6.3.

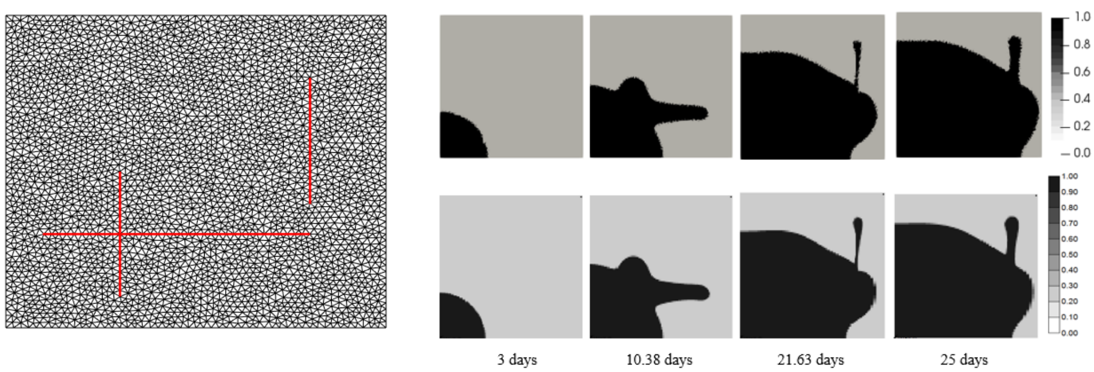

(a) (b)

Figure 4 (a) Computational mesh for the validation case of water-gas (two-phase) flow problem (red lines represent fractures); (b) Water saturation distributions at different times; the top four plots are predictions from the proposed model; the bottom four plots are predictions from commercial simulator (note that the color scales are slightly different, but only slight differences are detected between the two sets of results).

Validation Case 2 – McNamee-Gibson's problem. In the McNamee-Gibson's problem, deformation for when a constant strip load being applied on a poroelastic medium is considered (McNamee and Gibson, 1960a, b). There is an instantaneous fluid pressure buildup once the load is applied. **Table 1** summarizes the parameters used in this validation problem. The computational domain and boundary conditions are shown in **Figure 5(a)**, in which a piecewise traction is loaded on the top boundary, and fixed normal displacement boundaries are set for the left, right, and bottom boundaries. The observation point is located on the left boundary at a distance of 3.5 m below the top boundary. **Figure 5(b)** shows the comparison between numerical and analytical solutions for the pore pressure response in dimensionless form at the observation point. The good agreement among the two solutions validates the implementation of the presented coupled flow and geomechanical model following a fixed-stress splitting coupling scheme.

Table 1 Parameters used in McNamee-Gibson's validation problem

Parameters	Value	Unit
Model dimension	110×110	m
Porosity	0.25	–
Permeability	50	mD
Young's modulus	450	MPa
Poisson's ratio	0	–
Biot's coefficient	1	–
Fluid compressibility	4×10^{-10}	Pa^{-1}
Fluid viscosity	10^{-3}	Pa·s
Traction T_1, range a	20, 4	MPa, m
Traction T_2, range a_2	10, 106	MPa, m
Initial pressure	10	MPa
Consolidation coefficient (c)	0.0213	m^2/s

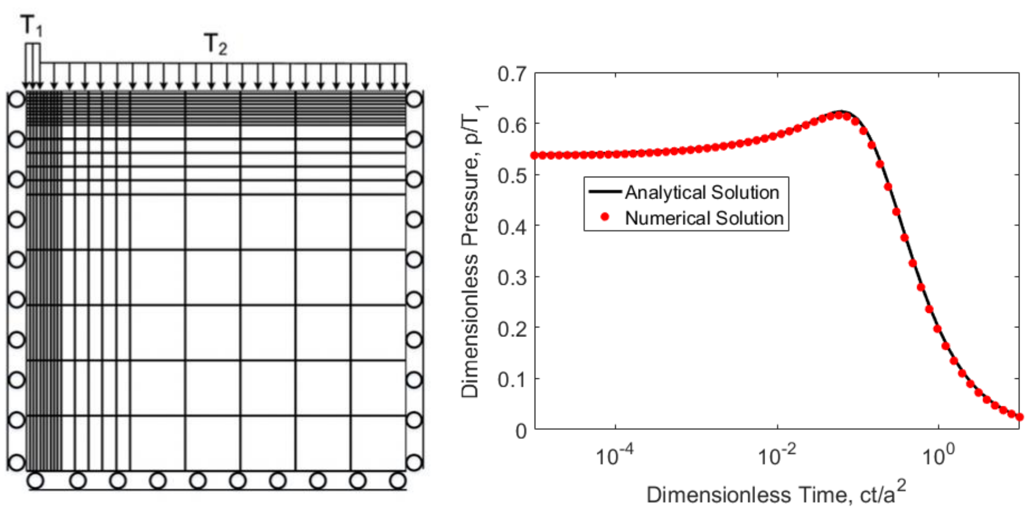

(a) (b)

Figure 5 (a) Computational domain and boundary conditions for the McNamee-Gibson's problem; (b) Comparison of pore pressure responses in dimensionless form at the observation point.

Fracturing Fluid Distribution Analysis

Simulation Model Setup

Coupled fluid flow and geomechanical simulation is performed to model fracturing fluid distribution and recovery. Explicit treatment of the discrete fractures with high spatial discretization resolution facilitates detailed examination of how fluids would distribute in the vicinity of fracture planes, such that any potential water blocking can be analyzed accurately. Four cases are examined next. First, a single planar fracture is placed in the middle of the domain to investigate the role of matrix imbibition on fracturing fluid distribution (Case 1). Moreover, to highlight the necessity of coupling with geomechanics, flow-only simulations are conducted based on the single fracture model. Next, three cases with complex fracture geometries are constructed (Case 2, Case 3 and Case 4) to examine the influences of natural or secondary fractures on the ensuing fluid distribution. Firstly, a stochastic fracture network is generated, of which the statistical parameters are listed in **Table 2**. In Case 2 and Case 3, it is assumed that the hydraulic fracture is deflected into natural fractures during the injection phase, resulting in fracture geometries with different degrees of complexity. The total water-filled fracture length of Case 3 is two times of that in Case 1 and Case 2. The total injection volume is kept constant for all cases while the water-filled fracture aperture is adjusted accordingly. The hydraulic fracture aperture is 0.01 m for Case 1 and Case 2, and 0.005 m for Case 3. For Case 4, it is assumed that the hydraulic fracture is connected with multiple gas-filled natural fractures. Since natural fractures not directly connected with hydraulic fractures have minimal impacts on fracturing fluid flowback (Yang et al. 2016), they are ignored in this study (i.e. only the natural fractures intersecting the hydraulic fracture are used in Case 4). **Figure 6** schematically illustrates the fracture geometry of each case. The model is initialized following the conditions described in Liu et al. (2018): the hydraulic fractures are initially filled with water with the pressure higher than the surrounding formation, mimicking the state right after the injection phase during a typical hydraulic fracturing treatment. No flow boundary condition is applied for the flow problem. For geomechanics, fixed normal displacement condition is applied to the left and bottom boundaries, while fixed traction condition is applied to the other two boundaries, and they are also schematically illustrated in **Figure 6**(a). Other relevant parameters are listed in **Table 3.**

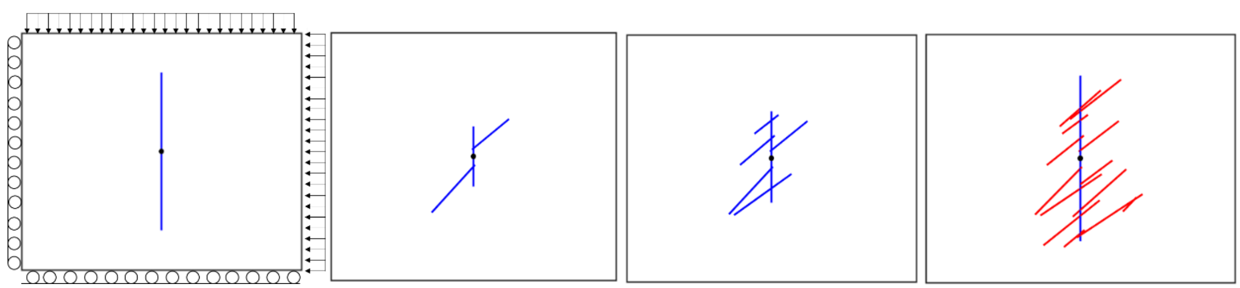

(a) (b) (c) (d)

Figure 6 Illustration of the computational domain (30 m × 30 m) and fracture geometry for cases 1-4 (blue line represents water-filled hydraulic fracture; red line represents gas-filled natural fracture; black dot indicates the perforation location). The same geomechanical boundary conditions, as illustrated in (a) is applied to all four cases.

Table 2 Statistical parameters of the generated natural fracture network.

Parameters	**Value**	**Unit**
Fracture density	1	m/m^2
Average fracture length	4	m
Average incline-angle	45	degree
Standard derivation of incline-angle	5	degree

Table 3 Summary of relevant parameters for the coupled flow and geomechanical simulation models.

Parameters	Value	Unit
Initial reservoir pressure	3.2×10^{7}	Pa
Initial natural fracture pressure	3.2×10^{7}	Pa
Initial hydraulic fracture pressure	5.5×10^{7}	Pa
Matrix porosity	0.06	–
Matrix permeability	2.0×10^{-19}	m^2
Matrix initial water saturation	0.25	–
Hydraulic fracture length	2	m
Hydraulic fracture porosity	0.9	–
Hydraulic fracture permeability	1.0×10^{-12}	m^2
Hydraulic fracture initial water saturation	1.0	–
Natural fracture aperture	0.001	m
Natural fracture porosity	0.5	–
Natural fracture permeability	1.0×10^{-14}	m^2
Natural fracture initial water saturation	0.1	–
Bottom-hole Pressure	2.0×10^{7}	Pa
Total in-situ stress	5.5×10^{7}	Pa
Young's modulus	29	GPa
Poisson's ratio	0.2	–
Biot's coefficient	0.7	–

The modified Brooks-Corey relations (Lake 1989; Brooks and Corey 1964) are used to generate the relative permeability and capillary pressure functions for the matrix, natural fracture and hydraulic fracture domains, as shown in **Figure 7** and **Figure 8**.

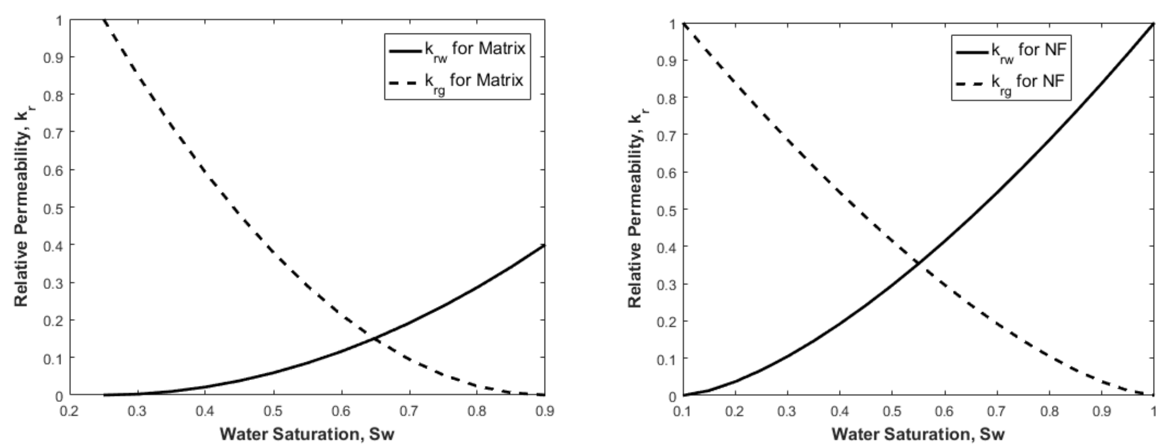

(a) (b)

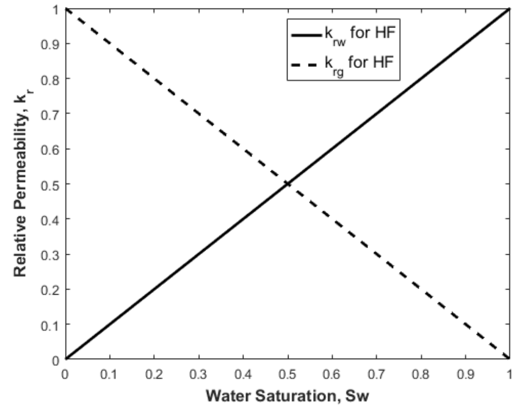

(c)

Figure 7 Relative permeability curves of matrix (a), natural fractures (b) and hydraulic fractures (c).

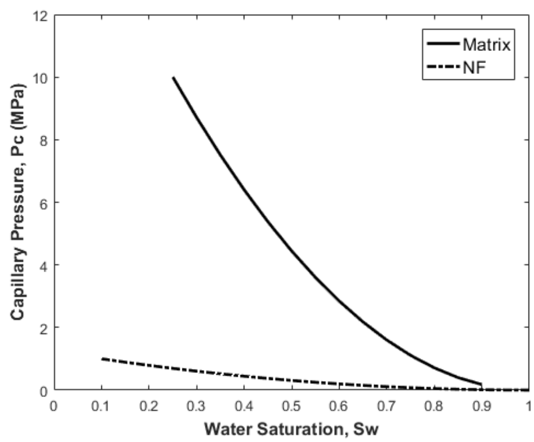

Figure 8 Capillary pressure curves of matrix and natural fractures.

Sensitivity Analysis – Results and Discussion

Single Planar Hydraulic Fracture. To assess the influences of geomechanical effects and matrix imbibition on fracturing fluid distribution and recovery, two sets of simulations are conducted with different shut-in durations (i.e. 1 day and 3 days): in one set, the flow problem is not coupled with geomechanical calculation; while in the other set of simulations, the coupled flow and geomechanical model is used. The water recovery factors under different conditions are compared in **Figure 9.** Clearly, the ultimate water recovery is lower when geomechanical effects are considered. This can be attributed to fracture closure, which hinders water flowing into the wellbore. Thus, coupled flow and geomechanics model should be considered when analyzing stress-sensitive fractured reservoirs. And the following discussions will be based on the results of coupled simulations.

As shown in **Figure 10** and **Figure 11**, fracturing fluid imbibes further into the matrix away from the hydraulic fracture faces as shut-in time increases. As expected, matrix imbibition is one of the major mechanisms for fracturing fluid loss, and this observation is corroborated by the trends of fracturing fluid recovery during flowback period in **Figure 9.** As the shut-in duration increases, the fracturing fluid recovery decreases, indicating that the imbibed fracturing fluid tends to remain in the matrix and potentially contributes to the so-called water blockage phenomenon that can be detrimental to long-term well productivity (Eveline et al. 2017; Liu et al. 2019; Wu et al. 2019). Comparing the water distribution profiles in **Figure 11** and **Figure 12**, it is clear that despite of a portion of the injected water being produced, the matrix water saturation near the hydraulic fracture remains high after the flowback period, which could significantly reduce the gas relative permeability and hinder efficient gas production. Removal of this water-blocking zone may potentially increase the well productivity, and surfactant-assisted EOR/EGR techniques (Longoria et al. 2017) may be suitable to reduce the nearby matrix capillary pressure. Resuming shut-in may allow the unrecovered fracturing fluid to continue imbibing into the matrix and to diffuse away from the near fracture region (Liu et al. 2019). However, this is a very slow process.

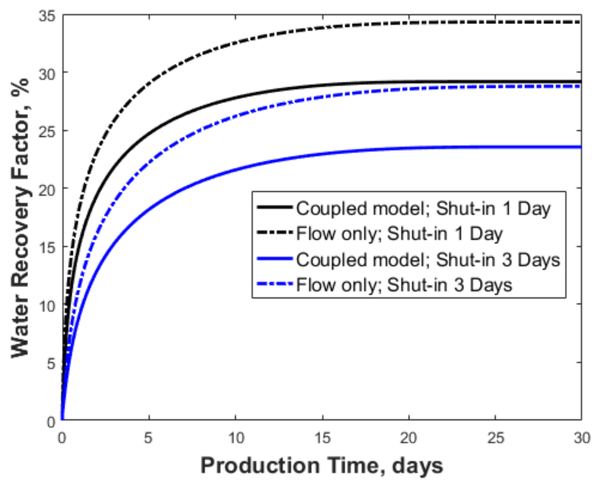

Figure 9 Comparison of water recovery factors with or without geomechanical coupling for two different shut-in times.

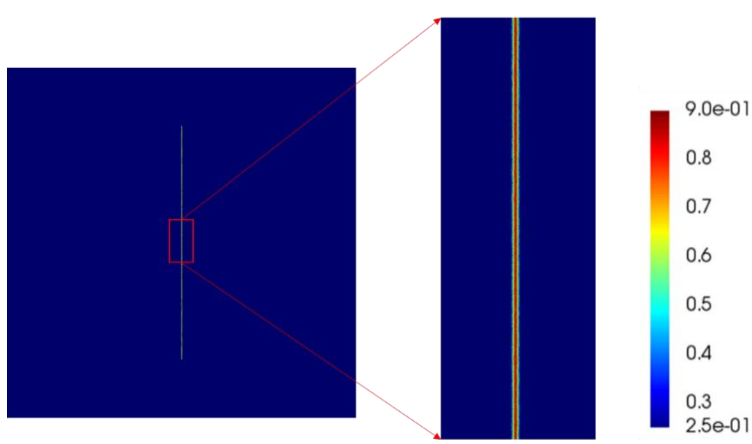

Figure 10 Water saturation distribution after a shut-in period of 1 day for Case 1.

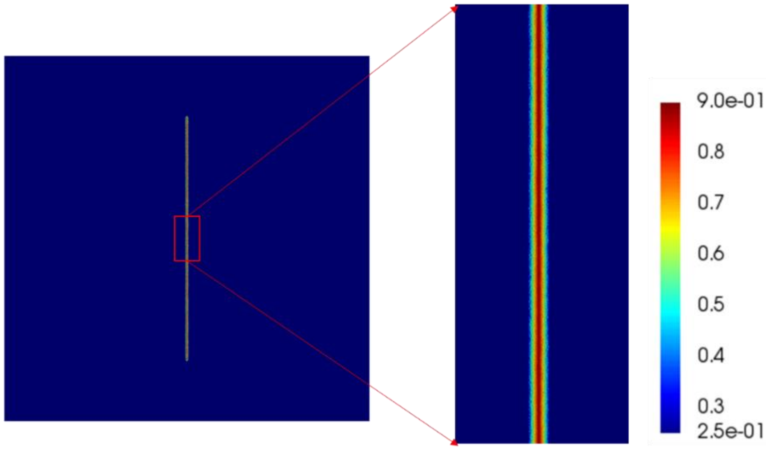

Figure 11 Water saturation distribution after a shut-in period of 3 days for Case 1.

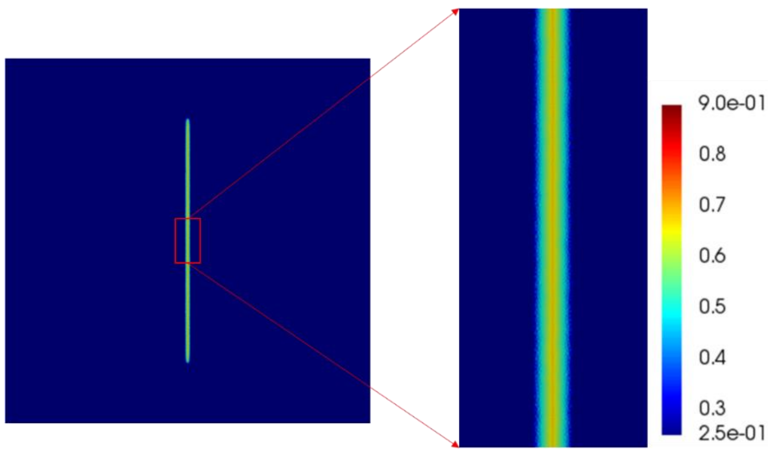

Figure 12 Water saturation distribution at the end of flowback for Case 1 with a shut-in period of 3 days.

Intersecting Hydraulic Fractures. More complex fracture configurations with intersecting fractures are studied in Case 2 and Case 3. The comparison between Case 1 and Case 2 is used to identify the impacts of fracture complexity on fracturing fluid flowback, while the comparison between Case 1 and Case 3 can help examine the influence of enlarged fracture interface on flowback behavior. With the same injection volume as for Case 1, the fracturing fluid distributions after different shut-in periods of 1 day and 3 days are shown in **Figure 13** and **Figure 14**, respectively. Once again, fracturing fluid imbibes into the surrounding matrix, and it should be noted that the water saturation is higher at the fracture intersecting point, since water from all fracture segments is accumulated at this point. **Figure 15** indicates the water recovery of Case 2 is slightly lower than that of Case 1 under the same shut-in time. The results indicate that the complexity of fracture geometry would affect water loss during flowback operations. This can be attributed to the tortuous nature of complex fracture geometries that reduces the water influx towards the wellbore.

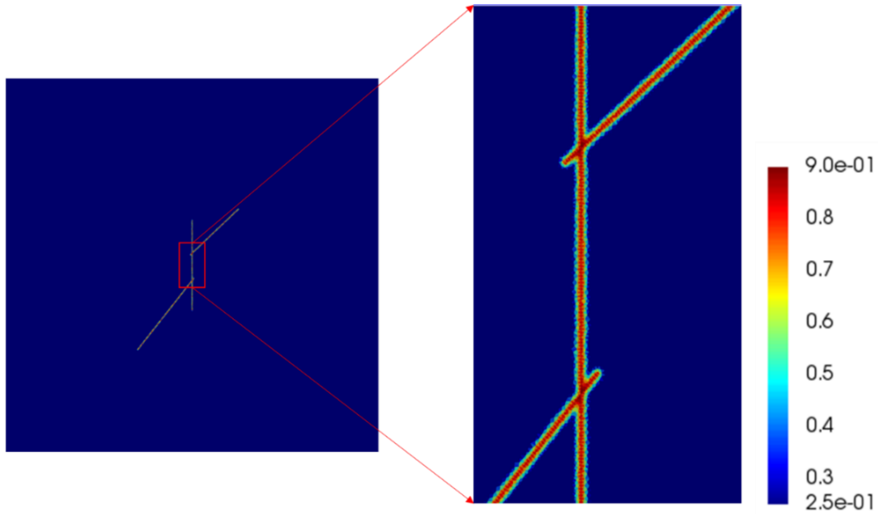

Figure 13 Water saturation distribution after a shut-in period of 1 day for Case 2.

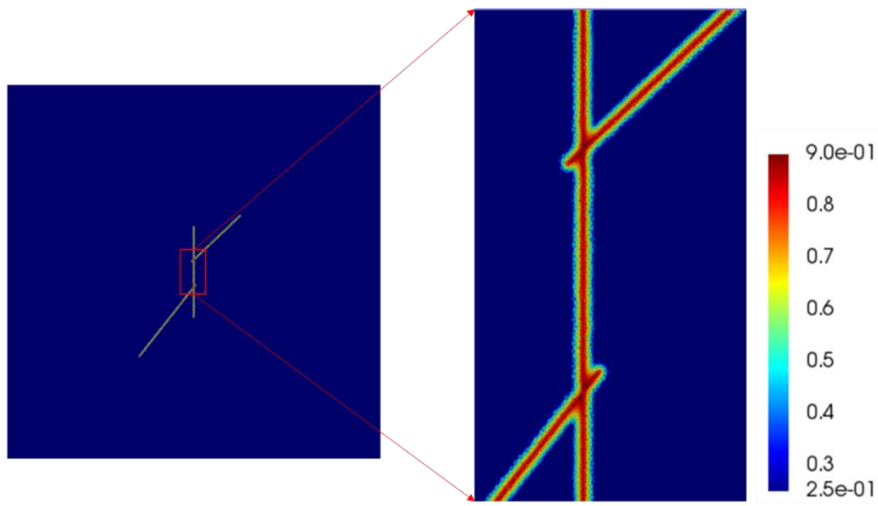

Figure 14 Water saturation distribution after a shut-in period of 3 days for Case 2.

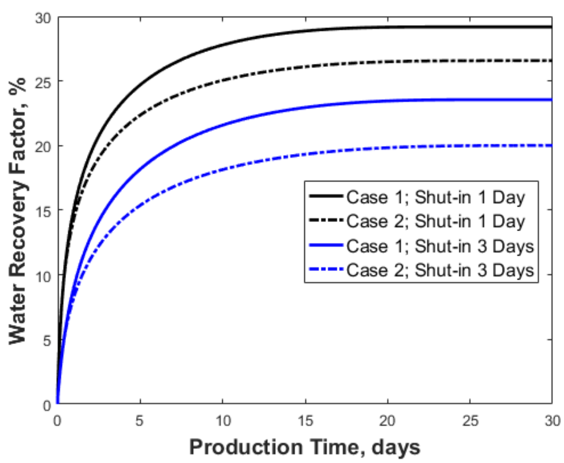

Figure 15 Fracturing fluid recovery factors (%) as a function of production time for Case 1 and Case 2 corresponding to different shut-in durations.

Similarly, **Figure 16** and **Figure 17** compare the fracturing fluid distribution of Case 3 after 1 day and three days shut-in, but the area of water invasion zone is increased for Case 3 due to its enlarged matrix-fracture interface. More water has imbibed into the matrix as compared to Case 1; therefore, the corresponding fracturing fluid recoveries are significantly reduced in Case 3, as illustrated in **Figure 18**. Moreover, time required to achieve maximum fracturing fluid recovery is shortened in Case 3 (i.e., the fracturing fluid has flown back faster in Case 3), which is due to the less mobile fracturing fluid in the fractures after the shut-in period.

These observations suggest that flowback characteristics (rate, volume and time) are potential indicators of the stimulated fracture geometry and area of the matrix-fracture interface. For instance, slightly lower fracturing fluid recovery, yet similar flowback time, may indicate a more complex fracture geometry than a simple planar fracture, despite of the identical total stimulated fracture length or total fracture-matrix interface area. On the other hand, significantly lower fracturing fluid recovery and shorter flowback time may designate a complex fracture geometry with enlarged fracture-matrix interface.

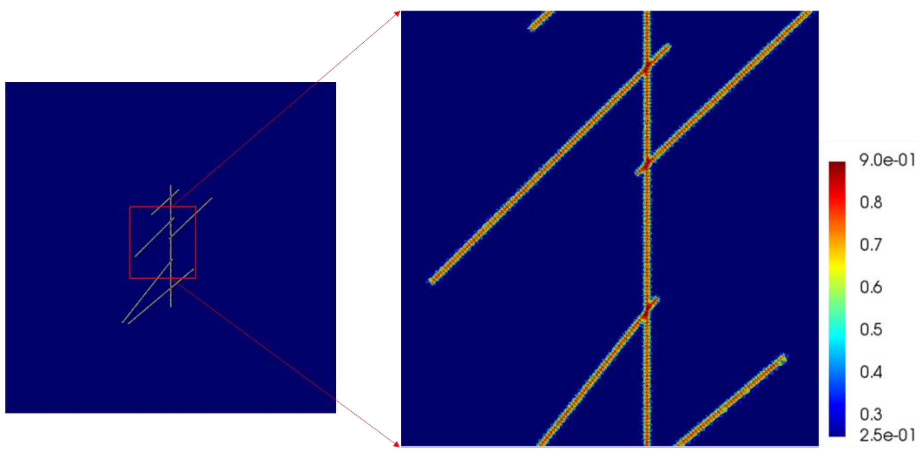

Figure 16 Water saturation distribution after a shut-in period of 1 day for Case 3.

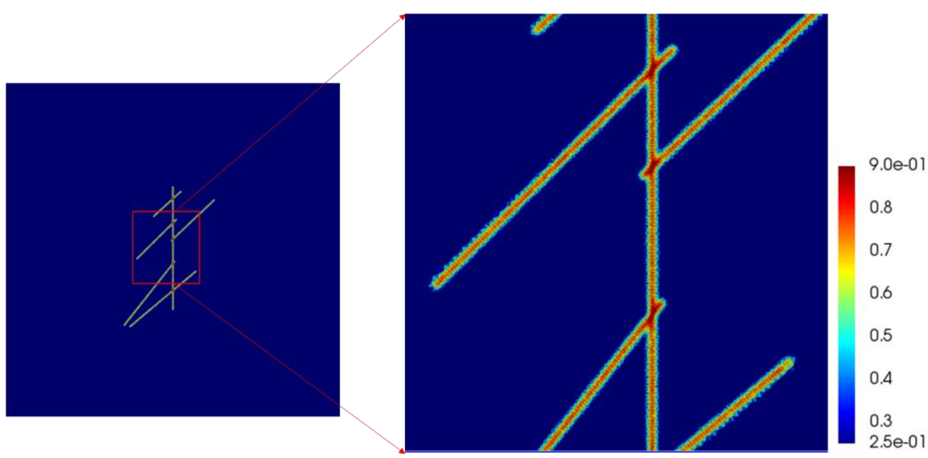

Figure 17 Water saturation distribution after a shut-in period of 3 days for Case 3.

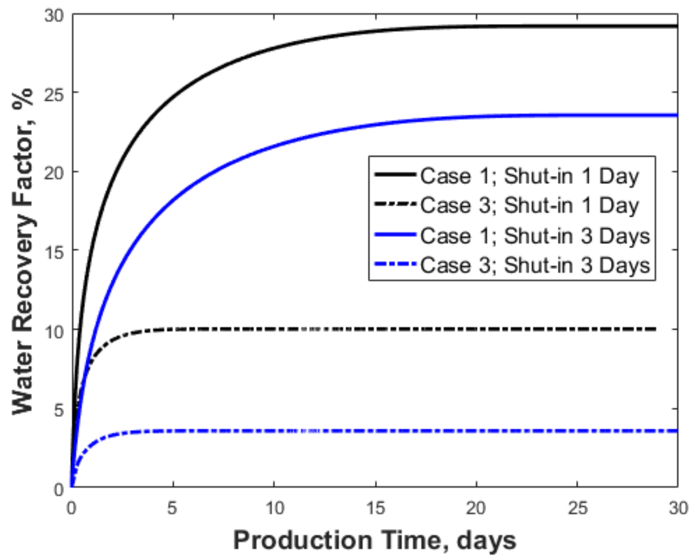

Figure 18 Fracturing fluid recovery factors (%) as a function of production time for Case 1 and Case 3 corresponding to different shut-in durations.

Natural Fractures. Given that natural fractures often exist in shale formations (Gale et al. 2014; Liu et al. 2019), the effects of natural fractures directly connected to the hydraulic fracture are examined in Case 4. The fracturing fluid distributions corresponding to different shut-in duration is analyzed. The results are similar to those of Case 1, with the exception that a portion of the fracturing fluid has temporarily leaked off into the natural fractures due to their relative high permeability, as compared with that of the matrix. The fluid then gradually imbibes into the nearby matrix, as shown in **Figure 19** and **Figure 20**. Comparing with the water recovery for Case 1, fluid leak-off into the nearby natural fractures leads to slightly lower fracturing fluid recovery, as shown in **Figure 21**. Moreover, the difference in ultimate water recovery between Case 1 and Case 4 increases as the shut-in time is extended, which also confirms the hypothesis that the existence of natural fractures may promote more water to imbibe into and be retained in the surrounding matrix. Another interesting observation is that, although the final water recovery is reduced in Case 4, the initial flowback rate of Case 4 is higher compared with Case 1. This is because the gas rate increases with the presence of natural fracture network, which displaces more water flowing into the wellbore, resulting in higher water flow rate. Correspondinly, the flowback time is also shortened due to the limited mobile fracturing fluid at the end of shut-in. Therefore, high initial flowback rate and short flowback time may be an indicator of existence of natural fractures directly connected to stimulated hydraulic fractures.

Moreover, **Figure 22** shows the water distribution after producing for 5 days (a) and 15 days (b) with a 3 days shut-in before flowback. Compared with the water distribution at the end of shut-in (**Figure 20),** the matrix water saturation near the fractures after producing 5 days (**Figure 22(a)**) becomes slightly higher which indicates that the remaining water in the fractures continues imbibing into the surrounding matrix under capillary drive. As production continues, water tends to flow further into the matrix, as evidenced by the expanded water invasion zone in **Figure 22(b)**. These observations support the hypothesis that unrecovered water would finally reside in the matrix due to strong capillarity, instead of being trapped in the fractures (assuming that these fractures do not close completely).

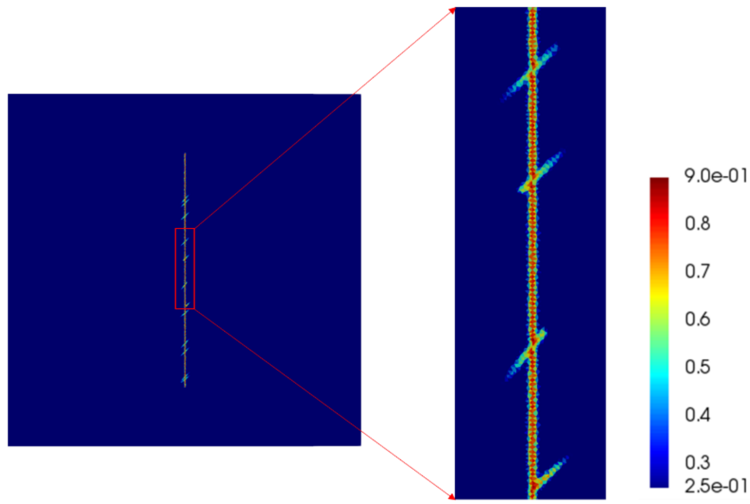

Figure 19 Water saturation distribution after a shut-in period of 1 day for Case 4.

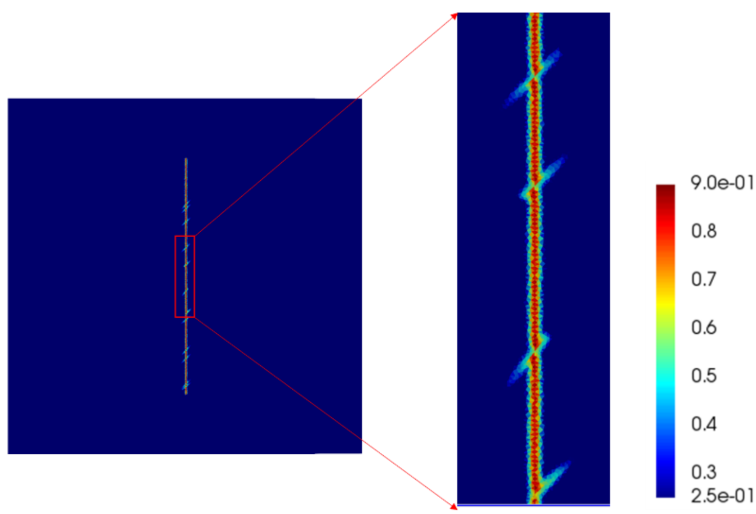

Figure 20 Water saturation distribution after a shut-in period of 3 days for Case 4.

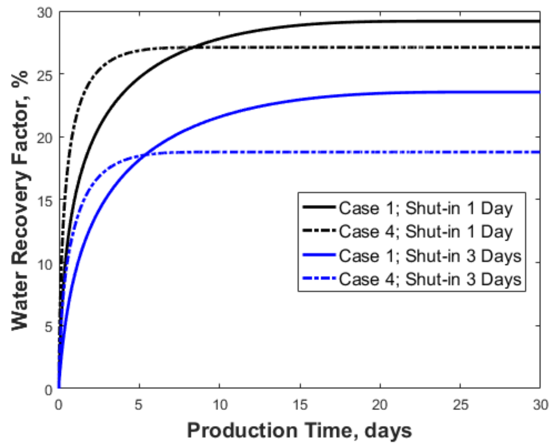

Figure 21 Fracturing fluid recovery factors (%) as a function of production time for Case 1 and Case 4 corresponding to different shut-in durations.

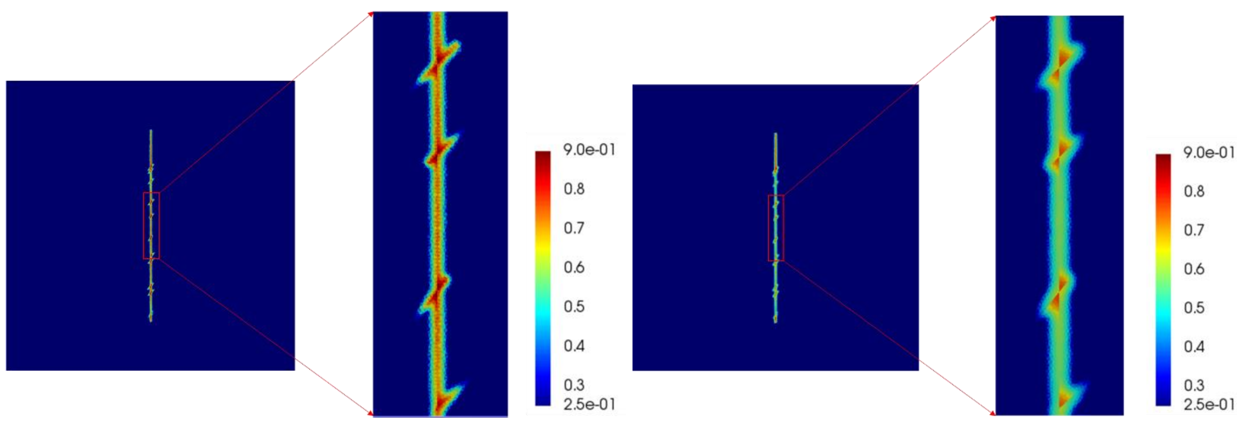

(a) (b)

Figure 22 Water distribution in the vinicity of fractures after a flowback duration of 5 days (a) and 15 days (b) with a period of 3 days shut-in before flowback.

The results for Case 4 seem to suggest that natural fractures could potentially act as conductive pathways that facilitate increased water imbibition into the surrounding matrix. However, natural fracture conductivity varies due to different degrees of mineralization or cementation (Gale et al. 2014). An additional scenario (Case 4a) is constructed, where the fracture permeability is increased to 50 mD. As shown in **Figure 23**, fracturing fluid leaks off further into the natural fractures in Case 4a with higher conductivity, compared with Case 4 in Figure 20. Correspondingly, as the natural fracture permeability increases, the fracturing fluid recovery factor decreases, as shown in **Figure 24**. The results support the postulation that high natural fracture conductivity would increase the overall permeability of the fractured medium, which, in turn, promotes water imbibition into the surrounding matrix. As a result, fluid leak-off characteristics could be indicators of the in-situ fracture configuration (geometries, intensities, and conductivities). Leak-off into the natural fractures may contribute to additional water loss; however, it is unlikely that water can be permanently trapped in the natural fractures without imbibing further into the matrix.

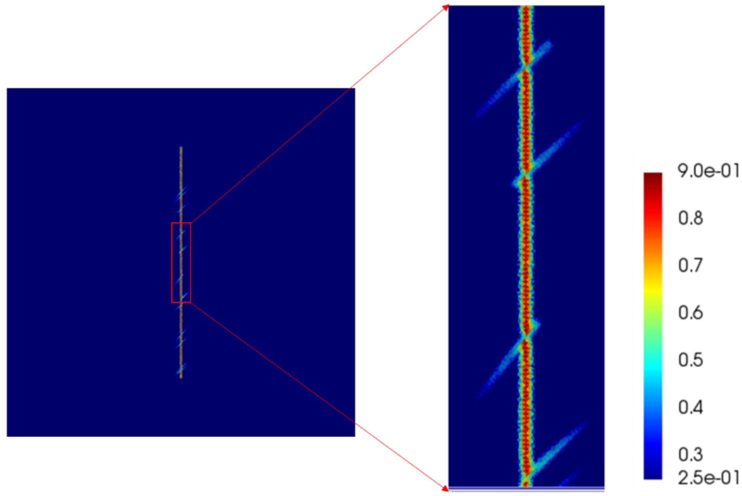

Figure 23 Water saturation distribution after a shut-in period of 3 days for Case 4a (i.e. high natural fracture conductivity).

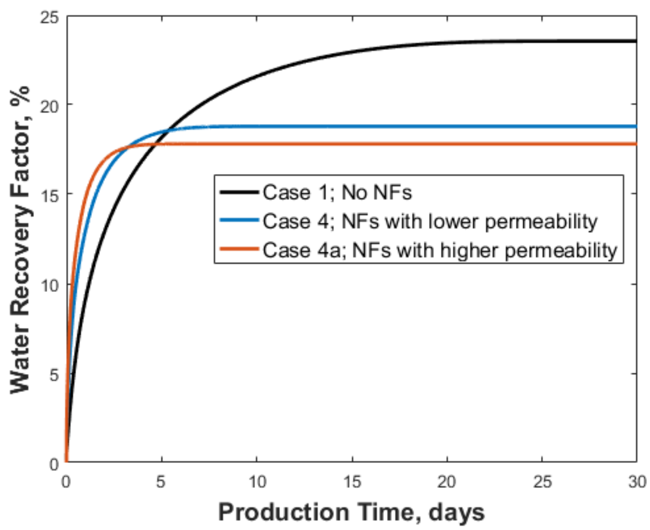

Figure 24 Fracturing fluid recovery as a function of production time for Case 1 (without NF), Case 4 (lower NF permeability) and Case 4a (higher NF permeability) after 3 days of shut-in time.

Conclusions

1. A sequential-implicit coupled two-phase flow and geomechanical simulation model incorporating a discrete fracture formulation is developed. The simulation model is validated against predictions from commercial simulator, as well as other existing or analytical solutions. The developed simulation model can be used to investigate coupled hydromechanical processes in fractured gas reservoirs.

2. The developed simulation model is used to predict fracturing fluid distribution and recovery profiles in fractured ultra-low permeability gas reservoirs. Discrete fractures are represented explicitly with high resolution. Matrix deformation, fracture closure and stress-dependent rock properties are coupled dynamically through poromechanics computations in the numerical

simulations. The focus is to visualize the temporal evolution of fracturing fluid distribution, as well as to explore the potential for inference of fracture geometry from flowback characteristics.

3. Matrix imbibition is the main controlling factor for water loss. Water invasion zone in the vicinity of hydraulic fractures increase with shut-in time. At the end of the flowback period, the matrix water saturation in areas close to the fracture face remains high, implying that water blocking may happen that inhibits gas flow.
4. Reservoirs with complex fracture geometries may exhibit low fracturing fluid recovery and shortened flowback time. Higher matrix water saturation is observed at the intersection of multiple fractures.
5. Leak off of fracturing fluid into natural fractures may contribute to water loss. However, this mechanism is strongly dependent on the natural fracture conductivity. Lower conductive natural fractures exhibit less impact on the fracturing fluid flowback behavior. It is unlikely that water can be permanently trapped in the natural fractures without imbibing further into the matrix.
6. This study aids in visualizing the detailed mechanisms associated with fracturing fluid distribution. It reveals various flowback characteristics that are related to the stimulated fracture geometry. More realistic (and complex) fracture geometry should be employed in future studies. Integrated fracture propagation and coupled simulation of flow-geomechanical processes is recommended.

Nomenclature

a_f	=	fracture aperture, m
A	=	interface area between elements, m^2
$\boldsymbol{C}$	=	elasticity tensor, Pa
D	=	distances from cell center to the centroid of shared interface, m
E_s	=	Young's modulus of proppant pack, Pa
m^k	=	Mass of component k, kg
$\boldsymbol{f}^k$	=	mass flux of component k, kg/(m^2·s)
F_f	=	fracture conductivity, m^3
q	=	source term, kg
$\boldsymbol{n}$	=	outer normal vector
S_J	=	saturation of phase J
ρ_J	=	density, kg/m^3
$\boldsymbol{w}_J$	=	mass flow of phase J, kg/s
μ_J	=	viscosity of phase J, Pa·s
k_r	=	relative permeability
$\boldsymbol{\sigma}$	=	stress tensor, Pa
$\boldsymbol{\varepsilon}$	=	strain tensor
$\boldsymbol{u}$	=	displacement vector, m
b	=	Biot's coefficient

ϕ	=	true porosity
ϕ^*	=	reservoir porosity
K_b	=	drained bulk modulus, Pa
K_s	=	modulus of solid grain, Pa
λ	=	fluid mobility, $Pa^{-1}\cdot s^{-1}$
ν	=	Poisson's ratio
Ω	=	computational domain
Γ	=	boundary of computational domain
$\boldsymbol{R}$	=	rotation matrix
$\boldsymbol{L}$	=	local displacement-separation matrix
$\boldsymbol{N}$	=	shape function matrix
$\boldsymbol{K}$	=	stiffness matrix, N/m
$\boldsymbol{f}$		traction vector, N

Acknowledgements

Y. Liu is thankful for the financial support of his work that was provided by the Texas Engineering Experiment Station and the Petroleum Engineering Department of Texas A&M University through their start-up funding of the projects of Prof. G. Moridis. Portions of this research were conducted with high performance research computing resources provided by Texas A&M University.

References

Abbasi, M.A., Ezulike, D.O., Dehghanpour, H. et al. 2014. A comparative study of flowback rate and pressure transient behavior in multifractured horizontal wells completed in tight gas and oil reservoirs. *Journal of Natural Gas Science and Engineering*, **17**: 82-93. http://dx.doi.org/10.1016/j.jngse.2013.12.007.

Alkouh, A., McKetta, S., Wattenbarger, R. A. 2014. Estimation of effective-fracture volume using water-flowback and production data for shale-gas wells. *Journal of Canadian Petroleum Technology*, **53**(05): 290-303.

Bertoncello, A., Wallace, J., Blyton, C. et al. 2014. Imbibition and water blockage in unconventional reservoirs: well management implications during flowback and early production. *SPE Reservoir Evaluation & Engineering*, **17**(04): 497-506. SPE-167698-PA. http://dx.doi.org/10.2118/167698-PA.

Biot, M.A., 1941. General theory of three-dimensional consolidation. *Journal of applied physics*, **12**(2): 155-164.

Brooks, R.H. and Corey, A.T., 1964. Hydraulic properties of porous media and their relation to drainage design. *Transactions of the ASAE*, **7**(1): 26-0028.

Cheng, Y. 2012. Impact of Water Dynamics in Fractures on the Performance of Hydraulically Fractured Wells in Gas-Shale Reservoirs. *Journal of Canadian Petroleum Technology* **51** (2): 143-151. SPE-127863-PA. http://dx.doi.org/10.2118/127863-PA.

Clarkson, C.R. and Williams-Kovacs, J., 2013. Modeling two-phase flowback of multifractured horizontal wells completed in shale. *SPE Journal*, **18**(04): 795-812. SPE-162593-PA. https://doi.org/10.2118/162593-PA

Computer Modeling Group (CMG). 2015. *GEM: Compositional & Unconventional Reservoir Simulator User's Guide, Version 2015, Calgary: CMG.*

Coussy, O., 2004. Poromechanics. John Wiley & Sons.

Dana, S., Ganis, B. and Wheeler, M.F., 2018. A multiscale fixed stress split iterative scheme for coupled flow and poromechanics in deep subsurface reservoirs. *Journal of Computational Physics*, **352**: 1-22.

Du, F. and Nojabaei, B. 2019. A Review of Gas Injection in Shale Reservoirs: Enhanced Oil/Gas Recovery Approaches and Greenhouse Gas Control. *Energies* **12** (12): 2355.

Ehlig-Economides, C.A. and Economides, M.J., 2011 Water as proppant. Presented at SPE Annual Technical Conference and Exhibition, Denver, Colorado, USA, 30 October-02 November. SPE-147603-MS. https://doi.org/10.2118/147603-MS

Eveline, V. F., Akkutlu, I. Y., and Moridis, G. J. 2017. Numerical Simulation of Hydraulic Fracturing Water Effects on Shale Gas Permeability Alteration. *Transport in Porous Media*, **116**(2): 727-752. https://doi.org/10.1007/s11242-016-0798-4

Fan, L., Thompson, J.W. and Robinson, J.R. 2010. Understanding gas production mechanism and effectiveness of well stimulation in the Haynesville Shale through reservoir simulation. Presented at the Canadian Unconventional Resources and International Petroleum Conference, Calgary, Alberta, Canada 19-21 October. SPE-136696-MS. http://dx.doi.org/10.2118/136696-MS.

Gale, J. F., Laubach, S. E., Olson, J. E. et al. 2014. Natural fractures in shale: A review and new observations. *AAPG bulletin*, **98**(11): 2165-2216. https://doi.org/10.1306/08121413151

Garipov, T.T., Karimi-Fard, M. and Tchelepi, H.A., 2016. Discrete fracture model for coupled flow and geomechanics. *Computational Geosciences*, **20**(1): 149-160.

Gdanski, R.D., Fulton, D.D. and Shen, C. 2009. Fracture-Face-Skin Evolution During Cleanup. *SPE Production & Operations*, **24** (01): 22-34. SPE-101083-PA. http://dx.doi.org/10.2118/101083-PA.

Geertsma, J., 1957. The effect of fluid pressure decline on volumetric changes of porous rocks.

Ji, L., Settari, A. and Sullivan, R.B., 2009. A novel hydraulic fracturing model fully coupled with geomechanics and reservoir simulation. *SPE Journal*, **14**(03): 423-430.

Jia, P., Cheng, L., Clarkson, C.R. and Williams-Kovacs, J.D. 2017. Flow behavior analysis of two-phase (gas/water) flowback and early-time production from hydraulically-fractured shale gas wells using a hybrid numerical/analytical model. *International Journal of Coal Geology*, **182**: 14-31.

Jiang, J. and Yang, J., 2018. Coupled fluid flow and geomechanics modeling of stress-sensitive production behavior in fractured shale gas reservoirs. *International Journal of Rock Mechanics and Mining Sciences*, **101**: 1-12.

Karimi-Fard, M., Durlofsky, L.J. and Aziz, K. 2004. An Efficient Discrete-Fracture Model Applicable for General-Purpose Reservoir Simulators. *SPE Journal*, **9**(02): 227-236.

King, G.E., 2010. Thirty years of gas shale fracturing: What have we learned?. Presented at the SPE Annual Technical Conference and Exhibition, Florence, Italy, 19-22 September. SPE-133456-MS. https://doi.org/10.2118/133456-MS

Kumar, A., Zorn, E., Hammack, R. et al., 2018. Long-period, long-duration seismic events and their probable role in reservoir stimulation and stage productivity. *SPE Reservoir Evaluation & Engineering*. SPE-191377-PA. https://doi.org/10.2118/191377-PA

Lake, L.W. 1989. Enhanced Oil Recovery, Chapter 3. Prentice Hall.

Li, J., Pei, Y., Jiang, H. et al. 2016. Tracer flowback based fracture network characterization in hydraulic fracturing. Presented at the Abu Dhabi International Petroleum Exhibition & Conference, UAE, 7-10 November. SPE-183444-MS.

Li, L., Pinprayong, V., Meng, F. et al. 2017. Fracture Network Evaluation Using Tracer Flowback: A Case Study. Presented at the SPE Symposium: Production Enhancement and Cost Optimisation, Kuala Lumpur, Malaysia, 7-8 November. SPE-189276-MS.

Liu, Y., Leung, J. Y. and Chalaturnyk, R. 2018. Geomechanical Simulation of Partially Propped Fracture Closure and Its Implication for Water Flowback and Gas Production. *SPE Reservoir Evaluation & Engineering*, **21**(02): 273-290.

Liu, Y., Leung, J.Y.W., Chalaturnyk, R.J. et al., 2019. New Insights on Mechanisms Controlling Fracturing-Fluid Distribution and Their Effects on Well Performance in Shale-Gas Reservoirs. *SPE Production & Operations*, **34**(3): 564-585.

Liu, L., Yao, J., Sun, H. et al. 2019. Compositional modeling of shale condensate gas flow with multiple transport mechanisms. *Journal of Petroleum Science and Engineering*, **172**, pp.1186-1201.

Longoria, R. A., Liang, T., Huynh, U. T. et al. 2017. Water blocks in tight formations: the role of matrix/fracture interaction in hydrocarbon-permeability reduction and its implications in the use of enhanced oil recovery techniques. *SPE Journal*, **22**(05): 1-393.

McNamee, J. and Gibson, R. E. 1960a. Displacement functions and linear transforms applied to diffusion through porous elastic media. *The Quarterly Journal of Mechanics and Applied Mathematics*, **13**(1): 98-111.

McNamee, J. and Gibson, R. E. 1960b. Plane strain and axially symmetric problems of the consolidation of a semi-infinite clay stratum. *The Quarterly Journal of Mechanics and Applied Mathematics*, **13**(2): 210-227.

Mikelić, A. and Wheeler, M.F., 2013. Convergence of iterative coupling for coupled flow and geomechanics. *Computational Geosciences*, **17**(3): 455-461. https://doi.org/10.1007/s10596-012-9318-y

Moridis, G.J., 2017. High Resolution Investigations of Flow and Thermal Processes During Production from Hydraulically Fractured Ultra-Low Permeability Media. Presented at the SPE Latin America and Caribbean Petroleum Engineering Conference, Buenos Aires, Argentina, 17-19, May. SPE-185512-MS. https://doi.org/10.2118/185512-MS

Mukuhira, Y., Dinske, C., Asanuma, H. et al. 2017. Pore pressure behavior at the shut-in phase and causality of large induced seismicity at Basel, Switzerland. *Journal of Geophysical Research: Solid Earth*, **122**(1): 411-435. https://doi.org/10.1002/2016JB013338.

Palisch, T.T., Vincent, M. and Handren, P.J., 2010. Slickwater fracturing: food for thought. *SPE Production & Operations*, **25**(03): 327-344. SPE-115766-PA. https://doi.org/ 10.2118/115766-PA

Park, K., and Paulino, G. H. 2012. Computational implementation of the PPR potential-based cohesive model in ABAQUS: Educational perspective. *Engineering fracture mechanics*, **93**: 239-262.

Rutqvist, J. and Stephansson, O., 2003. The role of hydromechanical coupling in fractured rock engineering. *Hydrogeology Journal*, **11**(1): 7-40. https://doi.org/10.1007/s10040-002-0241-5

Wang, J.Y., Holditch, S. and McVay, D. 2010. Modeling Fracture-Fluid Cleanup in Tight-Gas Wells. *SPE Journal*, **15** (03): 783-793. SPE 119624-PA. http://dx.doi.org/10.2118/119624-PA.

Wang, M. and Leung, J.Y. 2015. Numerical investigation of fluid-loss mechanisms during hydraulic fracturing flow-back operations in tight reservoirs. *Journal of Petroleum Science and Engineering*, **133:** 85-102. http://dx.doi.org/10.1016/j.petro.2015.05.013.

Wang, M. and Leung, J.Y., 2016. Numerical Investigation of Coupling Multiphase Flow and Geomechanical Effects on Water Loss During Hydraulic-Fracturing Flowback Operation. *SPE Reservoir Evaluation & Engineering*, **19**(03): 520-537.

Witherspoon, P. A., Wang, J. S., Iwai, K. et al. 1980. Validity of cubic law for fluid flow in a deformable rock fracture. *Water resources research*, **16**(6): 1016-1024.

Wu, Y., Cheng, L., Huang, S. et al. 2019. An analytical model for analyzing the impact of fracturing fluid-induced formation damage on rate transient behavior in tight formations. *Journal of Petroleum Science and Engineering*, **179**: 513-525.

Yan, X., Huang, Z., Yao, J. et al. 2018. An efficient numerical hybrid model for multiphase flow in deformable fractured-shale reservoirs. *SPE Journal*, **23**(04): 1-412.

Yang, R., Huang, Z., Li, G. et al. 2017. A semianalytical approach to model two-phase flowback of shale-gas wells with complex-fracture-network geometries. *SPE Journal*, **22**(06): 1-808.

Yue, M., Leung, J.Y. and Dehghanpour, H. 2016. Numerical Investigation of Limitations and Assumptions of Analytical Transient Flow Models in Tight Oil Reservoirs. *Journal of Natural Gas Science and Engineering*, **30**: 471-486. http://dx.doi.org/j.jngse.2016.01.042.